ApJ, in press, Jun 2012

The M31 Velocity Vector. II. Radial Orbit Towards the Milky Way and Implied Local Group Mass

Roeland P. van der Marel

Space Telescope Science Institute, 3700 San Martin Drive, Baltimore, MD 21218

Mark Fardal

Department of Astronomy, University of Massachusetts, Amherst, MA 01003

Gurtina Besla

Department of Astronomy, Columbia University, New York, NY 10027

Rachael L. Beaton

Department of Astronomy, University of Virginia, PO Box 3818, Charlottesville, VA 22903, USA

Sangmo Tony Sohn, Jay Anderson, Tom Brown

Space Telescope Science Institute, 3700 San Martin Drive, Baltimore, MD 21218

Puragra Guhathakurta

UCO/Lick Observatory, Department of Astronomy and Astrophysics, University of California at Santa Cruz, 1156 High Street, Santa Cruz, CA 95064

ABSTRACT

We determine the velocity vector of M31 with respect to the Milky Way and use this to constrain the mass of the Local Group, based on Hubble Space Telescope proper-motion measurements of three fields presented in Paper I. We construct N-body models for M31 to correct the measurements for the contributions from stellar motions internal to M31. This yields an unbiased estimate for the M31 center-of-mass motion. We also estimate the center-of-mass motion independently, using the kinematics of satellite galaxies of M31 and the

Local Group, following previous work but with an expanded satellite sample. All estimates are mutually consistent, and imply a weighted average M31 heliocentric transverse velocity of $(v_W, v_N) = (-125.2 \pm 30.8, -73.8 \pm 28.4)\ \mathrm{km\,s^{-1}}$. We correct for the reflex motion of the Sun using the most recent insights into the solar motion within the Milky Way, which imply a larger azimuthal velocity than previously believed. This implies a radial velocity of M31 with respect to the Milky Way of $V_{\mathrm{rad,M31}} = -109.3 \pm 4.4\ \mathrm{km\,s^{-1}}$, and a tangential velocity $V_{\mathrm{tan,M31}} = 17.0\ \mathrm{km\,s^{-1}}$, with 1σ confidence region $V_{\mathrm{tan,M31}} \leq 34.3\ \mathrm{km\,s^{-1}}$. *Hence, the velocity vector of M31 is statistically consistent with a radial (head-on collision) orbit towards the Milky Way.* We revise prior estimates for the Local Group timing mass, including corrections for cosmic bias and scatter, and obtain $M_{\mathrm{LG}} \equiv M_{\mathrm{MW,vir}} + M_{\mathrm{M31,vir}} = (4.93 \pm 1.63) \times 10^{12}\ \mathrm{M_\odot}$. Summing known estimates for the individual masses of M31 and the Milky Way obtained from other dynamical methods yields smaller uncertainties. Bayesian combination of the different estimates demonstrates that the timing argument has too much (cosmic) scatter to help much in reducing uncertainties on the Local Group mass, but its inclusion does tend to increase other estimates by $\sim 10\%$. We derive a final estimate for the Local Group mass from literature and new considerations of $M_{\mathrm{LG}} = (3.17 \pm 0.57) \times 10^{12}\ \mathrm{M_\odot}$. The velocity and mass results imply at 95% confidence that M33 is bound to M31, consistent with expectation from observed tidal deformations.

Subject headings: galaxies: kinematics and dynamics — Local Group — M31.

1. Introduction

The Milky Way (MW) is a member of a small group of galaxies called the Local Group (LG). The LG is dominated by its two largest galaxies, the MW and the Andromeda galaxy (M31). The mass and dynamics of this group have been the topic of many previous studies (e.g., van den Bergh 2000; van der Marel & Guhathakurta 2008, hereafter vdMG08; Li & White 2008; Cox & Loeb 2008; and references therein). Analysis of these topics is important for interpretation of structures inside the LG, such as dark halos, satellite galaxies, and tidal streams. It is also important for understanding the LG in a proper cosmological context, since it provides the nearest example of both Large Scale Structure and hierarchical galaxy formation. While much progress has been made in understanding the LG mass and dynamics, this has not been based on actual knowledge of the three-dimensional velocity vector of M31. This is because until now, the proper motion (PM) of M31 has been too small to measure

with available techniques.

In Paper I (Sohn, Anderson & van der Marel 2012) we reported the very first absolute PMs of M31 stars in three different fields observed with the Hubble Space Telescope (HST): a field along the minor axis sampling primarily the M31 spheroid (the "spheroid field"), a field along the major axis sampling primarily the M31 outer disk (the "disk field"), and a field along M31's Giant Southern Stream (GSS) sampling primarily the stars that constitute this stream (the "stream field"). For each field we measured the average PM of the M31 stars with respect to the stationary reference frame of background galaxies. The results are listed in Table 1. PMs in mas/yr were converted to velocities (v_W, v_N) in km/s in the directions of West and North using the known distance D of M31. Throughout this paper we adopt $D = 770 \pm 40$ kpc (see references in vdMG08). The velocity uncertainties are dominated by the PM uncertainties, with distance uncertainties making only a minimal contribution.

In the present paper we use the observed PMs to determine both the direction and size of the M31 velocity vector with respect to the MW, and we use this knowledge with the Local Group timing argument (Kahn & Woltjer 1959; vdMG08; and Li & White 2008) to estimate the LG mass. We then compare the velocity and mass results to independent estimates of the same quantities. For example, vdMG08 estimated the transverse motion of M31 based on the kinematics of satellite galaxies of M31 and the Local Group. Furthermore, the mass of the Local Group has been estimated independently by adding up the individual masses of the MW and M31, as estimated from various dynamical tracers (e.g. Klypin et al. 2002; Watkins et al. 2010). By statistically combining all the results we are able to build an improved and comprehensive understanding of the dynamics and mass of the LG.

The outline of this paper is as follows. In Section 2 we use N-body models of M31 and its prominent tidal substructures to calculate predictions for the *internal* kinematics of M31 stars in the three fields observed with HST. We use the results to correct the transverse velocities measured with HST, to estimate the transverse velocity of the M31 center-of-mass (COM). In Section 3 we revisit the methods of vdMG08 to estimate the M31 transverse motion from the kinematics of satellites, but with an expanded satellite sample. We combine the results with the HST measurements to obtain a final estimate for the M31 transverse motion. In Section 4 we derive the corresponding space motion in the Galactocentric rest frame, taking into account the latest insights about the solar motion in the MW. The results are consistent with a radial orbit for M31 towards the MW. In Section 5 we use the M31 motion to estimate the LG mass using the timing argument. We find that the estimate is quite uncertain due to cosmic scatter, and we show how a more accurate estimate can be obtained by combining it with estimates of the individual MW and M31 masses. In Section 6 we consider the galaxy M33, the third most massive galaxy of the Local Group (van den Bergh 2000), and

we derive its relative velocity with respect to M31. We also derive an estimate for the mass of M33, and show that M33 is most likely bound to M31, as is usually assumed. We use this knowledge to further refine our estimate for the Local Group mass. In Section 7 we discuss and summarize the main results of the paper. An Appendix presents a discussion of various parameterizations used in the literature (and the paper text) to quantify the dark halo density profiles and masses of galaxies. Where necessary to compare the properties of Local Group galaxies with predictions from cosmological simulations, we use a Hubble constant $H_0 = 70\,\mathrm{km\,s^{-1}\,Mpc^{-1}}$ and a matter density $\Omega_m = 0.27$ (Jarosik et al. 2011).

This is the second paper in a series of three. Paper III (van der Marel et al. 2012, in prep.) will present a study of the future orbital evolution and merging of M31, M33, and the MW, using the velocities and masses derived in the present paper as starting conditions.

2. Correction for Internal Kinematics

The PMs measured with HST in M31 fields contain contributions from both the M31 COM motion, and from the internal kinematics of M31. In each field, different fractions of the stars are contributed by different structural components. Specifically, the galaxy has different equilibrium components, including both a disk and spheroids (bulge/halo). We will refer to these jointly as the "base galaxy". The galaxy also contains material that is in the process of being accreted. This includes in particular the material responsible for the creation of the GSS (which in fact is spread out over a large fraction of the projected area of the galaxy, and not just the actual position of the Stream). To estimate the M31 COM motion, we need to know for each field observed with HST both the fraction of the stars in each component, and the transverse motion kinematics of those stars. The fractional contributions can in principle be estimated purely observationally from line-of-sight (LOS) velocity studies. However, estimates of the transverse motion kinematics requires a full dynamical model, since these motions are not directly constrained observationally. We therefore resort to N-body models for M31 like those previously constructed by some of us (e.g., Geehan et al. 2006; Fardal et al. 2006, 2007, 2008) to understand various observed features of M31.

2.1. N-body models of M31 Structure

The M31 model we use here is constructed from two separate but related parts. The base galaxy is an N-body realization of a model of the mass and light in M31 itself. The GSS component is a snapshot from a dynamical N-body simulation of the formation of the

GSS, performed using the same mass model of M31. Taken together, these two components reproduce reasonably well the features in M31 that are expected to contribute to our HST fields.

The base galaxy, which is a slightly altered version of the model from Geehan et al. (2006), contains bulge, disk, and halo components. The bulge and disk are assumed to be mostly baryonic and therefore trace the light. To the dark halo present in Geehan et al. (2006) we add a stellar halo, which is necessary to reproduce the extended power-law component that has been discovered in the halo regions (Guhathakurta et al. 2005; Irwin et al. 2005; Kalirai et al. 2006b; Chapman et al. 2006; Ibata et al. 2007). We assume this stellar halo follows the mass distribution of the dark halo, although it contains only a tiny fraction of that mass. When added together, these components satisfy the surface-brightness profiles of M31's bulge, disk, and halo regions reasonably well. Most importantly for this study, they also satisfy a series of kinematic constraints, including the disk rotation curve, the bulge velocity dispersion, and constraints on the halo mass from statistical tracers such as globular clusters, planetary nebulae, satellite galaxies, and red giant stars. We created the particle realization of this model using the ZENO library (Barnes 2011).

The GSS component is created by simulating the disruption of a satellite galaxy, in a fixed potential corresponding to the mass model just discussed. The model is an updated version of that found in Fardal et al. (2007), to which we refer the reader for a physical discussion. This model uses a spherical progenitor, although it is possible that the progenitor may in fact have been a disk galaxy (Fardal et al. 2008). After starting at large radius with carefully chosen initial conditions, the satellite disrupts at its first pericentric passage. The model is evolved using the PKDGRAV tree N-body code (Stadel 2001) for nearly 1 Gyr, until it forms orbital wraps closely resembling features in M31 including the GSS itself, and the NE and W shelves. We refer to all the particles generated by this component as the GSS component, regardless of where they are on the sky.

All the parameters of the base model, N-body simulations, and data-model comparisons are presented in Fardal et al. (2012, in prep.). However, many properties and details are similar to preceding papers (Geehan et al. 2006; Fardal et al. 2006, 2007, 2008). Besides the morphological evidence, the GSS model satisfies a set of observational constraints, including the detailed kinematic pattern in the W Shelf, the precise sky position of the GSS, the distance to various fields along the GSS (McConnachie et al. 2003), and their peak LOS velocities (Ibata et al. 2004; Guhathakurta et al. 2006; Kalirai et al. 2006a; Gilbert et al. 2009). We do not use the observed color-magnitude diagrams (CMDs) of the HST PM fields to constrain the models, since those are not easily decomposed into distinct structural components. In fact, the CMDs of the HST spheroid field and the HST stream field are strikingly similar,

given that they are believed to be dominated by different structural components (Brown et al. 2006).

Figure 1 shows a smoothed projected view of the N-body model. The GSS is visible South-East of the galaxy center, and the North-East and Western shelf are emphasized with dashed outlines. This image can be compared to star-count maps of giant stars in M31, which show the same features (e.g., Ibata et al. 2005; Gilbert et al. 2009; or Paper I, which also shows the location of our PM fields). Figure 2 shows a smoothed view of the N-body model in LOS velocity vs. projected distance space, for particles South-East of the galaxy center. There is good agreement between the outline of the GSS in this representation (dark band in the figure), and the observed peak LOS velocity of the GSS as a function of radius (blue points), including that measured in the HST stream PM field of Paper I (circle).

2.2. Proper-Motion Corrections for HST Fields

The predictions of the N-body model for M31 are summarized in Table 1 for each of the three HST fields. The quantity $f_{\rm base}$ is the fraction of the stars that belongs to the base galaxy, and $f_{\rm GSS}$ is the fraction of the stars that belongs to the GSS. The average velocities in the LOS, W, and N directions are listed for both the base and the GSS components, and also for their properly weighted average ("all"). The quantities were extracted over fields that are somewhat larger than the HST fields (up to 10 arcmin from the field center), to decrease the N-body shot noise. All velocities are expressed in a reference frame in which M31 is at rest.

The average internal transverse velocity kinematics of the M31 stars in the HST fields $(v_W, v_N)(all)$ are generally small, always below 125 km/s in absolute value. There are several reasons for this. In the HST spheroid field we are sampling primarily the spheroidal components of M31. At large radii these have limited mean rotation (Dorman et al. 2012). In the HST disk field we are primarily sampling the M31 disk, which has a sizeable circular velocity ($\sim$ 250 km/s). However, M31 has a large inclination. So along the major axis, most of the rotation is seen along the LOS, and not in the transverse direction. In the HST stream field we are primarily sampling the GSS, which has a significant mean three-dimensional velocity (254 km/s). However, the inclination of the stream is such that most of the velocity is seen along the LOS. Moreover, some 20% of the stars in the stream field do not belong to the GSS, but mostly to the spheroid component.

For all three fields, the contribution to the observed transverse motion from the internal kinematics of M31 is similar to or smaller than the random errors in the HST measurements.

Even significant fractional changes in the model predictions therefore do not strongly affect our final results. It therefore did not seem worthwhile in the context of the present study to further refine the model. Nonetheless, it is worth pointing out that the model is far from perfect, and that there are some salient features of M31 that it fails to reproduce. For example, the model with a spherical progenitor overestimates the contribution of GSS particles on their first orbital wrap to fields along the minor axis (especially those more distant than our spheroid field). Also, LOS velocity studies of the GSS have revealed a secondary cold component (in addition to the GSS and base galaxy; e.g., Kalirai et al. 2006a; Gilbert et al. 2007, 2009) which is not reproduced by our model. This could be, e.g., from a severely warped disk component, or from wrapped-around material of a GSS loop not included in our model. And finally, some authors have proposed models for the structure of M31's outer and accreted components that differ from those in our models (e.g., Ibata et al. 2005; Gilbert et al. 2007).

To estimate the transverse M31 COM motion from the data for each HST field, we first subtract the contribution from internal M31 kinematics ($v(all)$) from the measurement ($v(HST)$). We then correct for the effect of viewing perspective as described in van der Marel et al. (2002) and vdM08. This corrects for the fact that at the position of each field, the M31 COM systemic LOS and transverse velocity, respectively, are not exactly aligned along the *local* LOS and transverse directions. The corrections are small (below 10 km/s in absolute value), because all fields are located within 2 degrees of the M31 center. The final estimates are listed in Table 1 as $(v_W, v_N)(COM)$, and are summarized also at the top of Table 3. In propagating the uncertainties, we assigned an uncertainty of 20 km/s per coordinate to the model of the M31 internal kinematics. This number need not be known accurately, since the final uncertainties are always dominated by measurement errors in the PMs.

The results for the three different fields are mutually consistent with each other at the 1σ level (see also Paper I[1]). This justifies the use of a straightforward weighted average to combine the results, which gives $(v_W, v_N)(COM) = (-162.8 \pm 47.0, -117.2 \pm 45.0)$ km/s. For comparison, the direct weighted average of the HST observations, with no corrections for internal M31 kinematics, is $(v_W, v_N)(HST) = (-154.1 \pm 44.9, -112.9 \pm 42.9)$ km/s. Clearly, the corrections for internal kinematics make only a small difference for the final transverse velocity estimate. The fact that the differences are below 10 km/s is due to our combination of results for well-chosen fields, since the per-field corrections are much larger than this.

[1]Paper I defines a χ^2 quantity, χ^2_3, that assesses the extent to which measurements for different fields agree. Table 3 implies $\chi^2_3 = 3.5$, for $N_{\rm DF} = 4$ degrees of freedom.

3. Transverse Velocity from Satellite Kinematics

In vdMG08 we presented several methods for estimating the space motion of M31 from the kinematics of satellites, which assume that the satellites of M31 and the LG on average follow their motion through space. The M31 transverse velocity derived in that paper has random error bars of 34 to 41 km/s. This is somewhat smaller than what we have obtained here from the HST PM measurements, although the systematic error bars on the vdMG08 values may be larger (because the underlying methodology makes more assumptions). Either way, these results remain of considerable interest as an independent constraint on the M31 space motion. We therefore update here the results from vdMG08 using additional satellite data that has become available more recently.

3.1. Constraints from Line-of-Sight Velocities of M31 Satellites

The first method of vdM08 is based on the fact that any transverse motion of M31 induces an apparent solid body rotation in the line-of-sight velocity field of its satellites, superposed on their otherwise primarily random motions. The amplitude and major axis of the rotation field are determined by the size and direction of M31's transverse motion. In vdM08 we constrained the M31 transverse motion by fitting the velocities of 17 M31 satellites with known line-of-sight velocities.

For the present study we added the satellites listed in Table 2. These are objects that previously either did not have LOS velocity measurements available, or which had not yet been discovered. This includes six dSph galaxies: And XI, XIII, XV, XVI, XXI, and XXII. Three other recently discovered dSph galaxies, And XVII, XIX, XX, have not yet had their LOS velocities measured. As in vdMG08, we leave out And XII and XIV, because their large negative LOS velocities with respect to M31 indicate that they may be falling into M31 for the first time (Chapman et al. 2007; Majewski et al. 2007). We also leave out the more recently discovered And XVIII, which may be too distant from M31 to be directly associated with it (McConnachie et al. 2008). We do include And XXII, even though it may be a satellite of M33 rather than M31 (Martin et al. 2009; Tollerud et al. 2012). We note that And IV is not included in our combined sample because it is a background galaxy (Ferguson et al. 2000), while And VIII is not a galaxy at all (Merrett et al. 2006). For all dSphs, including those from Paper I and not listed in Table 2, we used the newly measured LOS velocities from Tollerud et al. (2012), where available. Otherwise, the values listed in Paper I or the sources listed in Table 2 were used. Our new sample in Table 2 also includes the 8 globular clusters of M31 that lie at projected distances > 40 kpc and have known LOS velocities.

We repeated the vdMG08 analysis, using the combined sample of the 17 satellites in Table 1 of vdMG08 and the 14 satellites in Table 2. The implied space motion of M31 is listed in Table 3 in the row labeled "M31 satellites". The result for (v_W, v_N) differs from that derived in vdMG08 by $(-40.1, 13.4)$ km/s. This is considerably smaller than the error bars in the result of $(144.1, 85.4)$ km/s. The addition of the 14 new satellites has not decreased the error bars on the result. This is in part because most satellites are observed relatively close to M31, so that any solid-body rotation signal would be small. As before, the new result is roughly consistent at the 1σ level with zero transverse motion. So no solid-body rotation component is confidently detected, which in turn implies that M31 cannot have a very large transverse motion. The fits imply a one-dimensional velocity dispersion for the satellite sample of $\sigma_{\rm sat} = 84.8 \pm 10.6$ km/s. This is $8.5\,{\rm km\,s^{-1}}$ larger than the value derived in vdMG08, which again is within the uncertainties.

3.2. Constraints from Proper Motions of M31 Satellites

The second method of vdM08 is based on the M31 satellites M33 and IC 10. These galaxies have accurately known PMs from water-maser observations (Brunthaler et al. 2005, 2007). The three-dimensional velocity vectors of these galaxies give an estimate of the M31 space motion to within an accuracy of $\sigma_{\rm sat}$ per coordinate. Transplanting the M33 and IC 10 velocity vectors to the position of M31, followed by projection onto the local LOS, W, and N directions, yields the results listed in Table 3 in the rows labeled "M33 PM" and "IC 10 PM". These are identical to what was derived in vdMG08, but with slightly larger uncertainties (due to the increased estimate of $\sigma_{\rm sat}$).

3.3. Constraints from Line-of-Sight Velocities of Outer Local Group Galaxies

The third method of vdMG08 is based on the line-of-sight velocities of Local Group satellites that are not individually bound to the MW or M31. In vdMG08 the method was applied to 5 satellites (see their Table 2). The Cetus dSph (RA= 6.54597°, DEC= $-11.04432°$) was excluded because of lack of knowledge of its LOS velocity at the time. For the present study we have rerun the analysis including Cetus, using $v_{\rm LOS} = -87 \pm 2$ km/s from Lewis et al. (2007). Its distance $D = 755 \pm 23$ kpc (McConnachie et al. 2005) places Cetus at $D_{\rm bary} \approx 600\,$kpc from the Local group barycenter. With addition of the Cetus dSph to the vdMG08 analysis, the implied space motion of M31 is listed in Table 3 in the row labeled "Outer LG Galaxies". The result for (v_W, v_N) differs from that derived in vdMG08 by $(-14.9, -13.5)$ km/s. This is considerably smaller than the error bars in the result of

$(58.0, 52.5)$ km/s.

3.4. Comparison and Combination of Constraints

In general, modeling of satellite galaxy dynamics can be complicated for a variety of reasons, especially when the goal is to estimate galaxy masses: the satellite system may not be virialized, with continueing orbital evolution (Mateo et al. 2008) or infall (e.g., Chapman et al. 2007; Majewski et al. 2007); the distribution of satellite orbits may not be isotropic (e.g., Watkins et al. 2010); satellites on large-period orbits are not expected to be randomly distributed in orbital phase (e.g., Zaritsky & White 1994); satellites may have correlated kinematics (e.g., van den Bergh 1998); and the three-dimensional distribution of satellites may not be spherical (Koch & Grebel 2006) or symmetric (McConnachie & Irwin 2006). However, many of these potential issues do not affect the analysis that we have presented here and in vdMG08 to estimate the M31 transverse velocity. Sections 3.1 and 3.2 only assume that the M31 satellites are drawn from a distribution that has the same mean velocity as M31, and which has no mean rotation. Section 3.3 only assumes that the LG satellites are drawn from a distribution that has the same mean velocity as the LG barycenter. Virialized equilibrium, isotropy, random phases, or symmetry are not required. Nonetheless, there is always the possibility that residual systematics may have affected the results. To get a handle on this, we have compared in detail the results for the M31 transverse velocity from the different techniques.

The (v_W, v_N) for M31 inferred from the different methods in Sections 3.1–3.3 are in mutual agreement to within the uncertainties. The same was true also in the original analysis of vdMG08. Since the methods and the underlying data are quite different for the various estimates, this in itself is a direct indication that any residual systematics cannot be large. Since the results from the different methods are in agreement, it is reasonable to take their weighted average, as listed in Table 3. The result for (v_W, v_N) differs from that derived in vdMG08 by $(-19.0, -7.1)$ km/s. This is considerably smaller than the error bars in the result of $(40.7, 36.6)$ km/s, so the new analysis presented here has not significantly altered the results previously derived by vdMG08.

An even stronger check on any residual systematics is provided by Figure 3. It compares the weighted average of the HST PM measurements (with corrections for internal kinematics) from Section 2 (as listed in Table 3) with the weighted average from the updated vdMG08 analysis. The difference between these results is $(\Delta v_W, \Delta v_N) = (-65.8 \pm 62.2, -72.1 \pm 58.0)$. This means that the results are consistent within the uncertainties: the probability of a residual this large occurring by chance in a *two-dimensional* Gaussian distribution is 26%.

Since the methods employed are totally different, and have quite different scopes for possible systematic errors, this is very successful agreement. This suggests not only that there are no large residual systematics in the results from the satellite kinematics, but also that there are no large residual systematics in the M31 PM analysis. This is a very important cross-check, since the displacements on which our PM measurements are based are below 0.01 detector pixels (see Paper I for a detailed discussion of the systematic error control in the PM analysis).

Since the HST PM analysis and the satellite kinematics analysis yield statistically consistent results for the M31 transverse velocity, it is reasonable to take the weighted average of the results from the two methodologies. This yields

$$(v_W, v_N) = (-125.2 \pm 30.8, -73.8 \pm 28.4)\,\mathrm{km\,s^{-1}}, \tag{1}$$

as listed in the bottom row of Table 3 and shown in black in Figure 3. This is the final result that we use for the remainder of our analysis.

4. Space Motion

4.1. Galactocentric Rest Frame and Solar Motion

As in vdMG08, we adopt a Cartesian coordinate system (X, Y, Z), with the origin at the Galactic Center, the Z-axis pointing towards the Galactic North Pole, the X-axis pointing in the direction from the Sun to the Galactic Center, and the Y-axis pointing in the direction of the Sun's Galactic rotation. We choose the origin of the frame to be at rest (the Galactocentric rest frame), and we wish to calculate the velocity of galaxies in this frame. This requires knowledge of the solar velocity in the Milky Way, since the solar reflex motion contributes to any *observed* velocities (such as the *heliocentric* velocities listed in Table 3).

In vdMG08 we adopted the standard IAU values (Kerr & Lynden-Bell 1986) for the distance of the Sun from the Galactic Center $R_0 = 8.5$ kpc, and the circular velocity of the Local Standard of Rest (LSR), $V_0 = 220$ km/s. Neither of these quantities has historically been known particularly accurately though, and their exact values continue to be debated. Recently, a number of new methodologies have become available. These provide new insights into R_0 and V_0, and we therefore use the results from these studies here.

Some of the best constraints on R_0 now come from studies of the orbits of stars around the Sgr A* supermassive black hole. Gillessen et al. (2009) obtained $R_0 = 8.33 \pm 0.35$ kpc (consistent also with Ghez et al. 2008). Most of the available constraints on the velocity V_0 are actually constraints on the ratio V_0/R_0. The best constraint on this ratio now comes

from the observed PM of Sgr A*, since the black hole is believed to be at rest in the galaxy to within $\sim$ 1 km/s. Reid & Brunthaler (2004) obtained that $(V_0 + V_{\rm pec})/R_0 = 30.2 \pm 0.2\,{\rm km\,s^{-1}\,kpc^{-1}}$. Here $V_{\rm pec}$ is the peculiar velocity of the Sun in the rotation direction. In vdMG08 we adopted the solar peculiar velocity from Dehnen & Binney (1998). However, there is now increasing evidence that $V_{\rm pec}$ from that study (and other studies) is too small by $\sim$ 7 km/s. We adopt here the more recent estimates from Schönrich, Binney, & Dehnen (2010): $(U_{\rm pec}, V_{\rm pec}, W_{\rm pec}) = (11.1, 12.24, 7.25)$, with uncertainties of $(1.23, 2.05, 0.62)$ km s^{-1} (being the quadrature sum of the random and systematic errors). Combination of these results implies that $V_0 = 239.3 \pm 10.3$ km/s, significantly larger than the canonical IAU value of 220 km/s. The uncertainty is dominated entirely by the uncertainty in R_0, and the errors in V_0 and R_0 are highly correlated.

Observations of masers in high-mass star-formation regions in the MW have been used to argue independently for a value of V_0 in excess of the canonical $220\,{\rm km\,s^{-1}}$ (Reid et al. 2009). However, McMillan & Binney (2010) showed that these data by themselves do not strongly constrain the Galactic parameters. On the other hand, McMillan (2011) showed that when combined with the other constraints described above through detailed models, the maser data do help to constrain R_0 more tightly, and therefore V_0. He obtained: $R_0 = 8.29 \pm 0.16$ kpc and $V_0 = 239 \pm 5$ km/s. These are the values we adopt here.

4.2. M31 Space Motion

Based on the adopted M31 distance and solar parameters, the position of M31 in the Galactocentric rest frame is

$$\vec{r}_{\rm M31} = (-378.9, 612.7, -283.1)\ {\rm kpc}. \tag{2}$$

The velocity of the Sun projects to $(v_{\rm sys}, v_W, v_N)_\odot = (191.9, 142.5, 78.5)\,{\rm km\,s^{-1}}$ at the position of M31. Since one observes the reflex of this, these values must be *added* to the observed M31 velocities to obtain its velocity in the Galactocentric rest frame. The velocity vector corresponding to the observed COM LOS velocity $v_{\rm LOS} = -301 \pm 1\,{\rm km\,s^{-1}}$ (vdMG08) and the final weighted average (v_W, v_N) given in Table 3, transformed to the Galactocentric rest frame, is then

$$\vec{v}_{\rm M31} = (66.1 \pm 26.7, -76.3 \pm 19.0, 45.1 \pm 26.5)\ {\rm km\,s^{-1}}. \tag{3}$$

The errors (which are correlated between the different components) were obtained by propagation of the errors in the individual position and velocity quantities (including those for the Sun) using a Monte-Carlo scheme.

If the transverse velocity of M31 in the Galactocentric rest frame, $V_{\rm tan}$, equals zero, then M31 moves straight towards the Milky Way on a purely radial (head-on collision) orbit. This orbit has $(v_W, v_N)_{\rm rad} = (-141.5 \pm 3.0, -78.8 \pm 1.7)\,{\rm km\,s^{-1}}$ (this is approximately the reflex of the velocity of the Sun quoted above, because the lines from the Sun to M31 and from the Galactic Center to M31 are almost parallel). The listed uncertainty is due to propagation of the uncertainties in the solar velocity vector. The radial orbit is indicated as a starred symbol in Figure 3. The velocity $\vec{v}_{\rm M31}$ calculated in the previous paragraph corresponds to a total velocity

$$|\vec{V}_{\rm M31}| = 110.6 \pm 7.8\,{\rm km\,s^{-1}}. \tag{4}$$

The radial velocity component is

$$V_{\rm rad,M31} = -109.2 \pm 4.4\,{\rm km\,s^{-1}}, \tag{5}$$

and the tangential velocity component is

$$V_{\rm tan,M31} = 17.0\,{\rm km\,s^{-1}} \qquad (1\sigma \text{ confidence region} : V_{\rm tan,M31} \leq 34.3\,{\rm km\,s^{-1}}). \tag{6}$$

The uncertainties were calculated as in vdMG08, using a flat Bayesian prior probability for $V_{\rm tan}$. These results imply that the velocity of M31 is statistically consistent with a radial orbit at the 1σ level.[2]

It has been known for a long time that the transverse velocity of M31 is probably $V_{\rm tan,M31} \lesssim 200\,{\rm km\,s^{-1}}$. The large scale structure outside the LG does not provide enough tidal torque to have induced a much larger transverse motion, subsequent to the radial expansion started by the Big Bang (Gott & Thuan 1978; Raychaudhury & Lynden-Bell 1989). Li & White (2008) used the ΛCDM cosmological Millenium simulation to identify some thousand galaxy pairs that resemble the MW-M31 pair in terms of morphology, isolation, circular velocities, and radial approach velocity. The median tangential velocity of the pairs was $V_{\rm tan} = 86\,{\rm km\,s^{-1}}$, with 24% of the pairs having $V_{\rm tan} < 50\,{\rm km\,s^{-1}}$ (see their figure 6). Therefore, the observed M31 tangential velocity is somewhat below average compared to cosmological expectation, but it is not unusually low. The exact reason why the tangential velocity of the MW-M31 pair has ended up below-average is not clear, but it may be related to the details of the growth history and the local environment of the LG.

Peebles et al. (2001) showed that at values $V_{\rm tan,M31} \lesssim 200\,{\rm km\,s^{-1}}$, many velocities can be consistent with the observed positions and velocities of galaxies in the nearby Universe. Our

[2]If the IAU value $V_0 = 220$ km/s is used for the LSR circular velocity and the Dehnen & Binney (1998) values are used for the solar peculiar velocity (as in vdMG08), then a radial orbit has $(v_W, v_N)_{\rm rad} = (-126.6, -71.4)\,{\rm km\,s^{-1}}$. With these assumptions, the inferred velocity of M31 is still statistically consistent with a radial orbit at the 1σ level.

new observational result that $V_{\rm tan,M31} \leq 34.3\,{\rm km\,s^{-1}}$ at 1σ confidence therefore significantly reduces the parameter space of possible orbits. Peebles et al. (2011) recently proposed a model for the history and dynamics of the LG in which $V_{\rm tan,M31} = 100.1\,{\rm km\,s^{-1}}$ and $(v_W, v_N) = (-240.5, -63.1)\,{\rm km\,s^{-1}}$. This is inconsistent with our final velocity estimates at $> 3\sigma$ confidence.

5. Local Group Mass

The velocity vector of M31 with respect to the Milky Way constrains the mass of the Local Group through the so-called "timing argument" (Kahn & Woltjer 1959; Lynden-Bell 1981, 1999; Einasto & Lynden-Bell 1982; Sandage 1986; Raychaudhury & Lynden-Bell 1989; Kroeker & Carlberg 1991; Kochanek 1996). Recent applications of this method were presented in vdMG08 and Li & White (2008). In Section 5.1 we provide a revised estimate of the Local Group timing mass using the new insights into the M31 velocity vector from Section 4.2. In Section 5.2 we combine the result in statistical fashion with results from other independent methods for constraining the Local Group mass.

Different studies often quote different mass quantities. However, for proper use and comparison it is important to transform all measurements to a common definition. For each galaxy, the total mass is dominated by a very extended dark halo. Common characterizations of dark matter halos are summarized in Appendix A. The density profile is often modeled as an NFW profile (Navarro et al. 1997; eq. [A2]) or a Hernquist (1990; eq. [A8]) profile. The former has infinite mass, while the latter has finite mass M_H. Common characterizations of halo masses also include the virial mass $M_{\rm vir}$ enclosed within radius $r_{\rm vir}$ (eq. [A1]), the mass M_{200} enclosed within the radius r_{200} (eq. [A5]), or the mass $M(r)$ enclosed within some given physical radius r in kpc (eqs. [A3,A9]).

In our discussion of galaxy masses, we transform all results into $M_{\rm vir}$ estimates. The transformation requires knowledge of the density profile, which for this purpose we assume to be of the NFW form with known concentration $c_{\rm vir}$ (eq. [A3]). For the MW and M31 we take $c_{\rm vir} = 10 \pm 2$, based on a combination of specific models (Klypin et al. 2002; Besla et al. 2007), and cosmological simulation results (Neto et al. 2007; Klypin et al. 2011). This implies $M_{200}/M_{\rm vir} = 0.839 \pm 0.014$ (eq. [A7]).

5.1. Timing Argument

Under the assumption of Keplerian motion, the relative orbit of M31 and the MW is determined by four parameters: the total mass $M_{\rm tot}$; the semi-major axis length a (or alternatively, the orbital period T); the orbital eccentricity e; and the current position within the orbit, determined by the eccentric anomaly η. In turn, four observables are available to constrain the orbit: the current M31 distance D; the radial and tangential M31 velocities in the Galactocentric rest frame, $V_{\rm rad,M31}$ and $V_{\rm tan,M31}$; and the time t since the last pericenter passage, which should be equal to the age of the Universe $t = 13.75 \pm 0.11$ Gyr (Jarosik et al. 2011; when the matter of both galaxies originated together in the Big Bang). There are as many observables as unknowns, so the orbital parameters and $M_{\rm LG}$ can be determined uniquely. The implied value of $M_{\rm tot}$ is called the "timing mass". Most commonly, the relevant equations are solved under the assumption of a radial orbit ($e = 1$ and $V_{\rm tan,M31} = 0$), but this assumption is not necessary when a measurement of $V_{\rm tan,M31}$ is actually available (e.g., vdMG08).

For the M31 space motion derived above, the "timing mass" $M_{\rm tot,timing} = (4.27 \pm 0.53) \times 10^{12} {\rm M}_\odot$. When a radial orbit is assumed (which is consistent with the data) then $M_{\rm tot,timing} = (4.23 \pm 0.45) \times 10^{12}$ M$_\odot$ (this is somewhat smaller, because any transverse motion increases the timing mass). The listed uncertainties are the RMS scatter of Monte-Carlo simulations as in vdMG08, which take into account all the observational uncertainties. The black curve in the top panel of Figure 4 shows the complete probability histogram for the radial orbit case.

These timing mass results are about 1.0–1.3 $\times 10^{12}$ M$_\odot$ lower than what was obtained by, e.g., vdMG08 and Li & White (2008). This can be viewed as an improvement, since previous estimates of $M_{\rm tot}$ appeared anomalously high compared to independent estimates of the masses of the individual M31 and MW galaxies (as summarized in vdMG08). Some of the decrease in timing mass is due to the fact that $V_{\rm tan,M31}$ found here is slightly smaller than in vdMG08. However, most of the decrease in timing mass is not due to the new HST measurements, but due to the new values for the solar motion used here. The solar velocity in the Y-direction, $v_Y = V_0 + V_{\rm pec}$, is 251.2 km/s in our calculations here. By contrast, it was 26 km/s lower in the calculations of vdMG08. The Y component of the solar motion projects predominantly along the LOS direction towards M31, and not the W and N directions. The component of the solar motion in the LOS direction is therefore 20.2 km/s higher than what it was in vdMG08. As a consequence, in the Galactocentric rest frame, M31 approaches the MW with a radial velocity that is 20.2 km/s slower than what is was in vdMG08. This slower approach implies a lower timing mass.

The timing argument equations are based on a simple Keplerian formalism. To assess

how accurate this argument is in a cosmological context one must make comparisons to N-body simulations (Kroeker & Carlberg 1991). Li & White (2008) did this for the currently favored ΛCDM cosmology, using results from the Millennium simulation. They identified simulated galaxy pairs like the MW-M31 system, with known masses, and quantified the accuracy of the *radial orbit* timing argument. They found that the timing argument has very little bias, when viewed as an estimate of the sum $M_{\rm tot,200}$ of the galaxy's M_{200} values, but significant scatter. They quantified this "cosmic scatter", by averaging over pairs with all possible transverse velocities. However, not surprisingly, their Figure 6 shows that the scatter increase with $V_{\rm tan}$. Since we now know that M31 actually has a low value of $V_{\rm tan}$, it is more appropriate to quantify the cosmic scatter by restricting the statistics to pairs in the simulation with low $V_{\rm tan}$. We measured by hand from their Figure 6 all pairs with $V_{\rm tan} \leq 50$ km/s, and extracted the ratio $M_{\rm tot,200}/M_{\rm tot,timing}$. We folded the probability distribution of these ratios into our Monte-Carlo scheme for estimating the total mass from the radial orbit timing argument. This yields the estimate $M_{\rm tot,200} = (4.14 \pm 1.36) \times 10^{12}\,{\rm M}_\odot$, which has a three times larger uncertainty than what is implied by observational errors alone. This can be converted into an estimate for the summed virial masses using to formulae of Appendix A, which yields

$$M_{\rm tot,vir} = (4.93 \pm 1.63) \times 10^{12}\,{\rm M}_\odot \qquad \text{(timing argument)}. \tag{7}$$

This is our final estimate from the timing argument, which takes into account observational uncertainties, cosmic bias, and cosmic scatter. The red curve in the top panel of Figure 4 shows the complete probability histogram for $M_{\rm tot,vir}$.

5.2. Combination with Other Milky Way and M31 Mass Constraints

The best alternative method for estimating the mass of the Local Group is to add up estimates of the masses of the individual M31 and MW galaxies.[3] Estimates for the masses of these galaxies were already summarized in vdMG08, so here we highlight primarily some more recent results.

Watkins et al. (2010) studied the kinematics of M31 satellites and found that the mass within 300 kpc is determined fairly robustly, $M_{\rm M31}(300\,{\rm kpc}) = (1.40 \pm 0.43) \times 10^{12}\,{\rm M}_\odot$. The quoted uncertainty is the quadrature sum of the random error of $0.40 \times 10^{12}\,{\rm M}_\odot$, and a systematic uncertainty of $0.15 \times 10^{12}\,{\rm M}_\odot$ due to the assumed velocity anisotropy of the satellites.

[3]The other method of estimating $M_{\rm tot}$ from the size of the Local Group turn-around radius yields estimates that tend to be biased low. A radial infall model is generally assumed, which is almost certainly an oversimplification (see vdMG08).

There may be other systematic uncertainties in the analysis, but these are more difficult to quantify and are neglected here. At this mass and with the relevant halo concentrations, $M(300\mathrm{kpc})/M_{\mathrm{vir}} = 1.018 \pm 0.002$ (see Appendix A). Hence, $M_{\mathrm{M31,vir}} = (1.38 \pm 0.43) \times 10^{12}\,\mathrm{M}_\odot$. We use this to set a Gaussian probability distribution for $M_{\mathrm{M31,vir}}$ in our discussion below (blue curve in top panel of Figure 4). This is consistent with the study of Klypin et al. (2002), which folded in a wider range of observational constraints, and obtained successful models with dark halo masses $M_{\mathrm{M31,dark,vir}}$ of either $1.43 \times 10^{12}\,\mathrm{M}_\odot$ or either $1.60 \times 10^{12}\,\mathrm{M}_\odot$. This corresponds to a total mass of $M_{\mathrm{M31,vir}} = 1.52 \times 10^{12}\,\mathrm{M}_\odot$ or $1.69 \times 10^{12}\,\mathrm{M}_\odot$, respectively, after adding in also the combined stellar mass of the M31 disk and bulge. The Watkins et al. results are also consistent with the recent results of Tollerud et al. (2012). They applied a mass estimator calibrated on cosmological simulations to the M31 satellite kinematics and obtained $M_{\mathrm{M31,vir}} = 1.2^{+0.9}_{-0.7} \times 10^{12}\,\mathrm{M}_\odot$.

Watkins et al. (2010) showed that mass estimates for the mass of the MW from satellite kinematics are much more uncertain. This is due to the unknown velocity anisotropy, combined with the fact that we see most satellites almost radially from near the Galactic Center. Good mass estimates therefore need to fold in a more diverse set of observational constraints. Moreover, uncertainties are reduced significantly by assuming that the radial profile of the dark matter is known, and follows a cosmologically motivated parameterization. McMillan (2011) used such methods to obtain a dark halo mass $M_{\mathrm{MW,dark,200}} = (1.26 \pm 0.24) \times 10^{12}\,\mathrm{M}_\odot$. This corresponds to $M_{\mathrm{MW,dark,vir}} = (1.50 \pm 0.29) \times 10^{12}\,\mathrm{M}_\odot$. This is consistent with the study of Klypin et al. (2002), who favored $M_{\mathrm{MW,dark,vir}} = 1.0 \times 10^{12}\,\mathrm{M}_\odot$, but showed that reasonable models with $M_{\mathrm{MW,dark,vir}} = 2.0 \times 10^{12}\,\mathrm{M}_\odot$ can be constructed as well. Adding the combined stellar mass of the MW disk and bulge to obtain the total $M_{\mathrm{MW,vir}}$ adds $\sim 0.06 \times 10^{12}$ to these values. The rapid motion of the Magellanic Clouds and Leo I have been used to argue for masses at the high end of this range of values (e.g., Zaritsky et al. 1989; Shattow & Loeb 2008; Li & White 2008; Boylan-Kolchin et al. 2011). However, the underlying assumptions in these arguments cause significant uncertainties. Based on the range of results in the literature, we adopt here, fairly arbitrarily, a flat probability distribution for $M_{\mathrm{MW,vir}}$ between 0.75 and $2.25 \times 10^{12}\,\mathrm{M}_\odot$ (green curve in top panel of Figure 4). This distribution has the same mean ($1.50 \times 10^{12}\,\mathrm{M}_\odot$) as inferred by McMillan (2011), and the same dispersion ($0.43 \times 10^{12}\,\mathrm{M}_\odot$) as we use for M31, but with a broader, flatter shape.[4]

[4]There do exist models in the literature that yield or use higher mass estimates for M31 and the MW than we use here. This includes estimates based on halo occupation distributions (e.g., Guo et al. 2010) or the timing argument (e.g., Loeb et al. 2005; Cox & Loeb 2008). It should be kept in mind though that such estimates are statistical in nature. Cosmic scatter must therefore be taken into account, and this yields large uncertainties (e.g., Li & White 2008; Guo et al. 2010). It is therefore important that any mass estimate *for an individual galaxy*, as opposed to an ensemble of galaxies, also take into account the actually observed

We use the listed probability distributions for the individual M31 and MW masses as priors; this also sets a prior probability distribution for $M_{\rm tot,vir} \equiv M_{\rm M31,vir} + M_{\rm MW,vir}$ (magenta curve in top panel of Figure 4). We then fold in the timing argument results to determine posterior probability distributions, as follows. We draw a random mass from the probability distribution for $M_{\rm tot,vir}$ derived from the timing argument (red curve in top panel of Figure 4). We then draw a random $M_{\rm MW,vir}$ from its prior distribution. We then calculate the corresponding $M_{\rm M31,vir} = M_{\rm tot,vir} - M_{\rm MW,vir}$, and its probability p given the prior distribution for $M_{\rm M31,vir}$. This set of values is then accepted or rejected in Monte-Carlo sense, depending on the probability p. We thus build up posterior probability distributions for $M_{\rm MW,vir}$, $M_{\rm M31,vir}$, and $M_{\rm tot,vir}$, which are shown as dotted lines with the same colors in the bottom panel of Figure 4.

The posterior distribution for $M_{\rm M31,vir}$ is still roughly Gaussian, but its average has increased from $(1.38 \pm 0.43) \times 10^{12}\,{\rm M}_\odot$ to $(1.51 \pm 0.42) \times 10^{12}\,{\rm M}_\odot$. The posterior distribution for $M_{\rm MW,vir}$ is not flat like its prior, but skewed towards higher masses. Its average has increased from 1.50 to $1.63 \times 10^{12}\,{\rm M}_\odot$. The likelihood of MW and M31 masses at the low end of the prior distributions is significantly reduced in the posterior distributions. This is relevant, since some previously reported mass estimates do fall on this low-mass end (e.g., Evans et al. 2000; Ibata et al. 2004). At the best-estimate virial masses for the MW and M31, the corresponding virial radii are 308 kpc and 300 kpc, respectively (eq. [A1]). Since the distance between the galaxies is $D = 770 \pm 40$ kpc, the virial spheres are not currently overlapping.

The prior distribution for $M_{\rm tot,vir}$ corresponds to $(2.88 \pm 0.61) \times 10^{12}\,{\rm M}_\odot$, while its posterior distribution corresponds to $(3.14 \pm 0.58) \times 10^{12}\,{\rm M}_\odot$. Therefore, inclusion of the timing argument increases the estimate of the LG mass by only $\sim 9\%$, due to the large cosmic variance. Since this is considerably smaller than the prior uncertainties on $M_{\rm MW,vir}$ and $M_{\rm M31,vir}$, the timing argument does not in fact help much to constrain the total LG mass, beyond what we already know from the MW and M31 individually. We have found this to be a robust conclusion, independent of the exact probability distributions adopted for M31 and the MW, and independent of the exact solar and M31 motion adopted in the timing argument.

---

resolved properties, rotation curves, and satellite kinematics.

6. Mass Constraints from M33

The galaxy M33 is the most massive companion of M31 (e.g., van den Bergh 2000). In the past decade, evidence has been found from both HI (Braun & Thilker 2004) and star-count maps (McConnachie et al. 2009) for tidal features indicative of past interactions between these galaxies. Models for these features such as those presented by McConnachie et al. (2009) require that M33 be bound to M31.[5] The galaxy M33 is one of the few galaxies in the Local Group for which an accurate PM measurement is available from VLBA observations of water masers. Hence, combined with our new M31 results, the relative motion of M33 with respect to M31 is now known with reasonable accuracy (Section 6.1). The mass of M33 can also be estimated independently (Section 6.2). With knowledge of the relative velocity and mass, the assumption that M33 is bound to M31 can be used to further refine our understanding of the M31 mass, and hence the Local Group mass (Section 6.3).

6.1. M33 Space Motion

To establish the binding energy of the M31-M33 system, we need to know the current position $\vec{r}_{\rm M33}$ and velocity $\vec{v}_{\rm M33}$ of M33 in the Galactocentric rest frame. These were determined in similar fashion as for M31 (see Section 4.2), but now based on the following observables: a distance $D_{\rm M33} = 794 \pm 23\,{\rm kpc}$ (McConnachie et al. 2004), line-of-sight velocity $v_{\rm los,M33} = -180 \pm 1\ {\rm km\,s^{-1}}$ (vdMG08), and PM from water masers as measured by Brunthaler et al. (2005) and discussed in vdMG08. This yields $\vec{r}_{\rm M33} = (-476.1, 491.1, -412.9)\,{\rm kpc}$, and $\vec{v}_{\rm M33} = (43.1 \pm 21.3, 101.3 \pm 23.5, 138.8 \pm 28.1)\ {\rm km\,s^{-1}}$. The observational errors in the Galactocentric velocity of M33 are similar to those for M31 reported in Section 4.2.

The positions of the three galaxies MW, M31 and M33 define a plane in the Galactocentric rest frame. For simplicity, we will refer to this plane as the "trigalaxy plane". It is of interest for understanding the orbital evolution of the MW-M31-M33 system, to know how the M33 velocity vector is oriented with respect to this plane. To assess this, we introduce a new Cartesian coordinate system (X', Y', Z') based on the following definitions: the frame has the same origin as the (X, Y, Z) system (i.e., the Galactic Center); the X'-axis points from the origin to M31 at $t = 0$; the Y'-axis is perpendicular to the X'-axis, and points from M31 to M33 as seen in projection from the Galactic Center; and the Z'-axis is perpendicular to the X'- and Y'-axes in a righthanded sense. With these definitions, the trigalaxy plane is

[5] While the MW also has a massive companion, namely the Large Magellanic Cloud, it is unclear whether the galaxies in this pair form a bound system (Besla et al. 2007).

the (X', Y') plane. Hence, let us refer to the (X', Y', Z') system as the "trigalaxy coordinate system".

Based on the position vectors $\vec{r}_{\rm M31}$ and $\vec{r}_{\rm M33}$ from Sections 4.2 and 6.1, the unit vectors of the (X', Y', Z') system can be expressed in (X, Y, Z) coordinates as

$$\begin{aligned} \vec{u}_{X'} &= (-0.48958, 0.79153, -0.36577), \\ \vec{u}_{Y'} &= (-0.47945, -0.60013, -0.64029), \\ \vec{u}_{Z'} &= (-0.72632, -0.13810, 0.67331). \end{aligned} \tag{8}$$

If $\vec{r}$ is a vector expressed in Galactocentric (X, Y, Z) coordinates, then the corresponding vector $\vec{r}'$ expressed in the trigalaxy coordinate system is

$$\vec{r}' = (X', Y', Z') = (\vec{r} \cdot \vec{u}_{X'}, \vec{r} \cdot \vec{u}_{Y'}, \vec{r} \cdot \vec{u}_{Z'}), \tag{9}$$

where $\cdot$ denotes the vector inner product. We use equations (8,9) as the fixed definition of the (X', Y', Z') system throughout this paper, even when we vary the positions of the Sun, M31, and M33 within their observational uncertainties.

Observational uncertainties of $\sim$ 20–30km s^{-1} aside, the velocities of M31 and M33 in trigalaxy coordinates are $\vec{v}'_{\rm M31} = (-109.2, -15.5, -7.1)$km s^{-1} and $\vec{v}'_{\rm M33} = (8.3, -170.3, 48.2)$km s^{-1}. These vectors make angles with the (X', Y') plane of only $-3.7°$ and $15.8°$, respectively. By definition, the MW galaxy currently has zero velocity in the Galactocentric rest frame. However, the gravitational attraction from M31 and M33 will set it in motion with a velocity directed in the (X', Y') plane. Hence, all three galaxies start out in the (X', Y') plane, with velocity vectors that are close to this plane. This implies that the orbital evolution of the entire MW-M31-M33 system will happen close to the trigalaxy plane, with the "vertical" Z'-component playing only a secondary role. Detailed calculations of the future orbital evolution and merging of the MW-M31-M33 system are the topic of Paper III.

6.2. M33 Mass

The mass of M33 is not negligible with respect to that of M31. It is therefore necessary to know the mass of M33 to determine whether the M31-M33 system is bound. Corbelli (2003) modeled the rotation curve and mass content of M33. The rotation curve rises to ~ 130 km s^{-1} out to the last data point at 15 kpc. Since the data do not reveal a turnover in the rotation curve, both the halo concentration and virial mass are poorly constrained (Fig. 6b of Corbelli 2003). Moreover, the rotation field is complex with significant twisting (Corbelli & Schneider 1997). This complicates interpretation in terms of circular motion.

To estimate the M33 virial mass it is therefore necessary to use more indirect arguments. For this, we compare M33 to M31.

Corbelli (2003) used her rotation curve fits to estimate the mass-to-light ratio of the M33 disk. From this, she inferred a stellar mass 2.8–5.6 $\times 10^9$ $M_\odot$ at 3σ confidence.[6] Higher values correspond to a maximum-disk fit, while lower values correspond to a sub-maximal disk. Guo et al. (2010) instead used the observed $B-V$ color of M33 with stellar population model predictions to estimate the mass-to-light ratio. With an assigned uncertainty of 0.1 dex for this method, one obtains $(2.84 \pm 0.73) \times 10^9$ $M_\odot$. We combine these methods into a single rough estimate $M_{\rm M33,*} = (3.2 \pm 0.4) \times 10^9$ $M_\odot$.

For M31, Klypin et al. (2002) used rotation-curve fits to estimate both the disk and the bulge mass. The two models they present cover the ranges $M_{\rm M31,disk} = 7.0$–9.0×10^{10} $M_\odot$ and $M_{\rm M31,bulge} = 1.9$–2.4×10^{10} $M_\odot$. Upon subtraction of the gas mass of $\sim 0.6 \times 10^{10}$ (van den Bergh 2000), this yields $M_{\rm M31,*} = (8.3$–$10.8) \times 10^{10}$ $M_\odot$. The Guo et al. (2010) method based on the galaxy $B-V$ color yields instead $M_{\rm M31,*} = (7.0 \pm 1.8) \times 10^{10}$ $M_\odot$. We combine these methods into a single rough estimate $M_{\rm M31,*} = (7.9 \pm 0.9) \times 10^{10}$ $M_\odot$.

These estimates imply that $M_{\rm M33,*}/M_{\rm M31,*} = 0.041 \pm 0.007$. This can be compared to the *baryonic* mass ratio implied by the Tully Fisher relation, $(V_{\rm M33}/V_{\rm M31})^4$ (McGaugh 2005). With $V_{\rm M33} \approx 130\,{\rm km\,s^{-1}}$ (Corbelli & Salucci 2000) and $V_{\rm M31} \approx 250\,{\rm km\,s^{-1}}$ (Corbelli et al. 2010) this yields 0.073. This is consistent with the estimate of $M_{\rm M33,*}/M_{\rm M31,*}$, if one takes in to account that in M33 the stars make up only $\sim 57\%$ of the baryonic mass, the rest being mostly in neutral and molecular gas (Corbelli 2003).

Models of the halo occupation distribution of galaxies predict a relation for M_*/M_{200} as function of halo mass M_{200}, when matching observed galaxy properties from the Sloan Digitial Sky Survey to the properties of dark matter halos seen in simulations (e.g., Wang et al. 2006; Guo et al. 2010). From Section 5.2 we have $M_{\rm M31,vir} = (1.50 \pm 0.38) \times 10^{12}\,M_\odot$, which corresponds to $M_{\rm M31,200} = (1.26 \pm 0.32) \times 10^{12}\,M_\odot$. Combined with knowledge of the observed $M_{\rm M33,*}/M_{\rm M31,*}$, this can be used to estimate M_{200} for M33, and hence the virial mass.[7] This yields $M_{\rm M33,vir} = (0.170 \pm 0.059) \times 10^{12}$ $M_\odot$ based on the Guo et al. relations, and $M_{\rm M33,vir} = (0.127 \pm 0.055) \times 10^{12}\,M_\odot$ based on the Wang et al. relations. The uncertainties were estimated

[6] Corbelli's mass scale for $H_0 = 65\,{\rm km\,s^{-1}\,Mpc^{-1}}$ was transformed to the Hubble constant used here. The small mass contribution from the nuclear component of M33 is well within the quoted uncertainties. M33 has no bulge.

[7] In relating M_{200} to $M_{\rm vir}$ for M33, we assume that $c_{\rm vir} = 10 \pm 2$, as we did for the MW and M33. While the lower mass of M33 would in principle lead one to expect a higher concentration, this is not supported by fits to the rotation curve (Corbelli 2003).

using a simple Monte-Carlo scheme that includes, in addition to the observational errors, the Gaussian cosmic scatter of ~ 0.2 dex in stellar mass at fixed halo mass (Guo et al. 2010).[8] The difference in normalization between the predictions from Wang et al. and Guo et al. is not well understood. So we treat this as an additional model uncertainty, and allow all values bracketed between the two relations with equal probability. This yields as our final estimate $M_{\rm M33,vir} = (0.148 \pm 0.058) \times 10^{12}\ {\rm M}_\odot$.[9]

Strictly speaking, the mass inferred from halo occupation distributions is the so-called infall mass. Thus we assume that mass loss to M31 has not yet been significant. On the other hand, the uncertainty on $M_{\rm M33,vir}$ is significant. Also, our $M_{\rm M33,vir}$ estimate falls below what is implied by direct application of the Guo et al. relations. Therefore, significant mass loss would not be inconsistent with the range of masses we explore here.

6.3. Mass Implications of a Bound M31-M33 Pair

To assess the likelihood, given the data, that M31 and M33 are bound, we set up mass and velocity combinations in Monte-Carlo sense. The initial masses $M_{\rm vir}$ for both galaxies were drawn as in Sections 5.2 and 6.2. The initial phase-space coordinates were drawn as in Sections 4 and 6.1. This scheme propagates all observational distance and velocity uncertainties and their correlations, including those for the Sun[10]. For each set of initial conditions we calculated the binding energy of the M33-M31 system. The M33-M31 system was found to be bound in 95.3% of cases. Therefore, our observational knowledge of the masses, velocities, and distances of these two galaxies indicates that indeed, they most likely form a bound pair.

The observation of tidal features associated with M33 independently implies that M31 and M33 are likely a bound pair (Braun & Thilker 2004; McConnachie et al. 2009). If

[8]This exceeds the observational errors in M_* for both M33 and M31. As a result, it is not necessary for the present method to have particularly robust estimates of these observational uncertainties.

[9]We could instead have used the mass $M_{\rm M33,*}$ directly to estimate $M_{\rm M33,vir}$, with no reference to M31. This yields $M_{\rm M33,vir} = (0.225 \pm 0.055) \times 10^{12}\,{\rm M}_\odot$ based on the Guo et al. relations, and $M_{\rm M33,vir} = (0.123 \pm 0.034) \times 10^{12}\ {\rm M}_\odot$ based on the Wang et al. relations. Both of these estimates are consistent with what we use here. However, there is a significant difference in absolute mass normalization between the theoretical relations. The relations agree better in a relative sense, which is why we prefer the method used here. The latter uses only relative theoretical predictions, combined with the kinematically determined virial mass for M31.

[10]Uncertainties in the RA and DEC of M31 and M33 are negligible and were ignored.

we enforce this as a prior assumption, then this affects our posterior estimates of the M31 and M33 masses. To enforce this assumption, we merely need to remove from our Monte-Carlo scheme those initial conditions in which M33 and M31 are not bound. Figure 4b shows as solid histograms the posterior distributions after application of this additional prior. The main effect is to disallow some of the initial conditions in which $M_{\rm M31}$ (blue curve) is on the low end of its probability distribution. The average and RMS mass increase from $M_{\rm M31,vir} = (1.51 \pm 0.42) \times 10^{12}\,{\rm M}_\odot$ to $(1.54 \pm 0.39) \times 10^{12}\,{\rm M}_\odot$. The mass distribution of M33 is not appreciably affected. The posterior mass distribution for $M_{\rm tot,vir} = M_{\rm MW,vir} + M_{\rm M31,vir}$ is shown as the cyan histogram. Its average and RMS are

$$M_{\rm tot,vir} = (3.17 \pm 0.56) \times 10^{12}\,{\rm M}_\odot \qquad \text{(final estimate)}. \tag{10}$$

This is similar to the result from Section 5.2, which was $M_{\rm tot,vir} = (3.14 \pm 0.58) \times 10^{12}\,{\rm M}_\odot$. Hence, the assumption that M33 must be bound to M31 does not help much to reduce the uncertainties in the LG mass, since the fact that they are bound is already implied at high confidence by the observed velocities.

The probability distributions of M31 and M33 distances and velocities are not appreciably affected by the additional prior that M31 and M33 be bound. The average positions and velocities in the Galactocentric rest frame remain the same to within 1 kpc and a few km/s, respectively, after the unbound orbits are removed.

7. Discussion and Conclusions

We have presented the most accurate estimate to date of the transverse motion of M31 with respect to the Sun. This estimate was made possible by the first PM measurements for M31, made using HST, and presented in Paper I. We have combined these measurements with other insights to constrain the transverse motion of M31 with respect to the MW. We have used the resulting motion to improve our understanding of the mass of the Local Group, and its dominant galaxies M31 and the MW.

The HST PM measurements from Paper I pertain to three fields in M31. The PM for each field contains contributions from three components: the M31 COM motion, the known viewing perspective, and the internal kinematics of M31. To correct for the contributions from internal kinematics, we have constructed detailed N-body models. The models include both the equilibrium disk, bulge, spheroid, and dark-halo components, as well as the material from a tidally disrupted satellite galaxy that is responsible for the GSS. Even though the stars in M31 move at velocities of hundreds of km/s, the internal-kinematics corrections to the observed PMs averaged over all fields is quite small ($\lesssim 25\,{\rm km\,s^{-1}}$, well below the

random uncertainties in the measurements). This is largely due to the known properties of the carefully chosen field locations, and the galaxy components that they sample.

The resulting M31 transverse motion should be largely free from systematic errors, based on the many internal consistency checks built into our PM program, as discussed in Paper I. This includes the fact that the observations for the three different fields, including observations with different instruments at different times, all yield statistically consistent estimates for the M31 COM motion. Nonetheless, an entirely independent check on the results is obtained by comparison to the M31 transverse motion estimates implied by the methods from vdMG08, which are based exclusively on the kinematics of the *satellite galaxies* of M31 and Local Group.

Instead of using the published results from vdMG08 directly, we have redone their analysis using expanded satellite samples, including new data that has become available in recent years. The end result is similar to what was already published by vdMG08. More importantly, the result is statistically consistent with that obtained from the HST PM program. Since the methods employed are totally different, and have very different scopes for possible systematic errors, this is very successful agreement. This gives added confidence in both results, and also suggests that a further reduction in the uncertainties can be obtained by taking the weighted average of both methods. This yields $(v_W, v_N) = (-125.2 \pm 30.8, -73.8 \pm 28.4)$, which is our final estimate for the *heliocentric* transverse motion of M31. The uncertainties in this result are similar to what has been obtained from VLBA observations of water masers in the M31 satellites M33 and IC10 (Brunthaler et al. 2005, 2007).

To understand the motion of M31 with respect to the MW, it is necessary to correct for the reflex motion of the Sun. We adopted the most recent insights into the solar motion within the Milky Way. These imply an azimuthal motion for the Sun (the sum of the LSR motion and the solar peculiar velocity) of $\sim$ 250 km/s, which is $\sim$ 25 km/s higher than what has typically been used in previous studies. This implies a radial approach velocity of M31 with respect to the Milky Way of $V_{\rm rad,M31} = -109.2 \pm 4.4\,{\rm km\,s^{-1}}$, which is $\sim$ 20 km/s slower than what has typically been used in previous studies. The best estimate for the tangential velocity component is $V_{\rm tan,M31} = 17.0\,{\rm km\,s^{-1}}$, with 1σ confidence region $V_{\rm tan,M31} \leq 34.3\,{\rm km\,s^{-1}}$. Hence, the velocity of M31 is statistically consistent with a radial (head-on collision) orbit towards the MW at the 1σ level.

The new insights into the motion of M31 with respect to the MW allowed us to revise estimates of the Local Group timing mass, as presented most recently by vdMG08 and Li & White (2008). This yields $M_{\rm tot,timing} = 4.23 \times 10^{12}\,{\rm M_\odot}$ for an assumed radial orbit, with a random error from observational uncertainties of $0.45 \times 10^{12}\,{\rm M_\odot}$. This result is $\sim$ 20% lower than typically found in previous studies, due to the lower $V_{\rm rad,M31}$ used here. We

calibrated the timing mass as in Li & White (2008) based on cosmological simulations. However, we selected from their galaxy pairs in the Millennium simulation only those with low $V_{\rm tan,M31}$, for consistency with the observations. This yields $M_{\rm tot,vir} \equiv M_{\rm MW,vir} + M_{\rm M31,vir} = (4.93 \pm 1.63) \times 10^{12}\,{\rm M}_\odot$, where the uncertainty now includes cosmic scatter (which dominates over random errors).

We have presented a Bayesian statistical analysis to combine the timing mass estimate for $M_{\rm tot,vir}$ with estimates for the individual masses of M31 and the MW obtained from other dynamical methods. For the individual masses we used relatively broad priors that encompass most values suggested in the literature. Even then, the cosmic scatter in the timing mass is too large to help much in constraining the mass of the Local Group. Its main impact is to increase by $\sim 10\%$ the mass estimates already known for the individual galaxies (and their sum).

In an attempt to further refine the M31 and Local Group mass estimates, we have studied the galaxy M33. Its known PM allowed us to study the relative motion between M31 and M33. A range of arguments suggests that the mass of M33 is $\sim 10\%$ of the M31 mass. The masses and relative motions of M31 and M33 indicate that they are a bound pair at 95% confidence. Observational evidence for tidal deformation between M33 and M31 suggests that the small 5% probability for unbound pairs, as allowed by the observational uncertainties, may not be physical. This makes low values for the M31 mass unlikely, and hence increases the expectation value for the Local Group mass, but only by $\sim 1\%$. Our final estimate for the Local Group mass from all considerations is $M_{\rm tot,vir} = (3.17 \pm 0.57) \times 10^{12}\,{\rm M}_\odot$.

The velocity vectors between M31, M33 and the MW are all closely aligned with the plane that contains these galaxies. Paper III presents a study of the future orbital evolution and merging of these galaxies, using the velocities and masses derived here as starting conditions.

Support for Hubble Space Telescope proposal GO-11684 was provided by NASA through a grant from STScI, which is operated by AURA, Inc., under NASA contract NAS 5-26555. The PKDGRAV code used in Section 2.1 was kindly made available by Joachim Stadel and Tom Quinn, while the ZENO code used in that section was kindly made available by Josh Barnes. The authors are grateful to T. J. Cox for contributing to the other papers in this series, and to the anonymous referee for useful comments and suggestions.

A. Dark Halo Profiles, Masses, and Sizes

Spherical infall models show that a virialized mass $M_{\rm vir}$ has an average overdensity $\Delta_{\rm vir}$ compared to the average matter density of the Universe. The virial radius $r_{\rm vir}$ therefore satisfies $\overline{\rho}_{\rm vir} \equiv 3M_{\rm vir}/4\pi r_{\rm vir}^3 = \Delta_{\rm vir}\Omega_m\rho_{\rm crit}$, or in physical units (Besla et al. 2007)

$$r_{\rm vir} = 206h^{-1}\ {\rm kpc}\left(\frac{\Delta_{\rm vir}\Omega_m}{97.2}\right)^{-1/3}\left(\frac{M_{\rm vir}}{10^{12}h^{-1}\ {\rm M}_\odot}\right)^{1/3}. \tag{A1}$$

For the cosmological parameters used here, $h = 0.7$ and $\Omega_m = 0.27$, one has $\Delta_{\rm vir} = 360$ (Klypin et al. 2011).

Dark halo density profiles in cosmological simulations are well described by an NFW density profile (Navarro et al. 1997),

$$\rho_N(r) = \rho_s x^{-1}(1+x)^{-2}, \qquad x \equiv r/r_s. \tag{A2}$$

The enclosed mass is

$$M_N(r) = 4\pi\rho_s r_s^3 f(x) = M_{\rm vir} f(x)/f(c_{\rm vir}), \qquad f(x) = \ln(1+x) - \frac{x}{1+x}, \tag{A3}$$

where the concentration is defined as $c_{\rm vir} = r_{\rm vir}/r_s$. The average enclosed mass density equals

$$\overline{\rho}_N(r) \equiv 3M_N(r)/4\pi r^3 = 3\rho_s(r_s/r)^3 f(x). \tag{A4}$$

Another characteristic radius that is often used is the radius r_{200} so that the average enclosed density is 200 times the critical density of the Universe, $\overline{\rho}_{200} \equiv 3M_{200}/4\pi r_{200}^3 = 200\rho_{\rm crit}$, where M_{200} is the enclosed mass. It follows from the respective definitions that

$$q \equiv \overline{\rho}_{200}/\overline{\rho}_{\rm vir} = (200/\Delta_{\rm vir})\Omega_m^{-1}, \tag{A5}$$

which yields $q = 2.058$ for the cosmological parameters used here. This exceeds unity, and therefore $r_{200} < r_{\rm vir}$ and $M_{200} < M_{\rm vir}$. For the NFW profile, r_{200} is the solution of the equation $\overline{\rho}_N(r_{200}) = q\overline{\rho}_N(r_{\rm vir})$, which implies

$$c_{200}/c_{\rm vir} = \left(\frac{f(c_{200})}{qf(c_{\rm vir})}\right)^{1/3} \tag{A6}$$

where $c_{200} \equiv r_{200}/r_s$. This equation can be quickly solved numerically using fixed point iteration, starting from an initial guess for c_{200} on the right hand side. The corresponding mass ratio is

$$M_{200}/M_{\rm vir} = f(c_{200})/f(c_{\rm vir}). \tag{A7}$$

As discussed in Springel et al. (2005), it is often convenient for numerical reasons to model dark halos with a Hernquist (1990) profile. This is what we will do in our exploration of the orbital evolution of the MW-M31-M33 system in Paper III. In this case the density profile is

$$\rho_H(r) = \left(\frac{M_H}{2\pi a^3}\right) y^{-1}(1+y)^{-3}, \qquad y \equiv r/a. \tag{A8}$$

Here M_H is the total mass of the system, which is finite, unlike for the NFW profile. The enclosed mass is

$$M_H(r) = M_H y^2 (1+y)^{-2}. \tag{A9}$$

The Hernquist profile has the same density as the NFW profile for $r \to 0$ if

$$M_H = 2\pi \rho_s a^2 r_s. \tag{A10}$$

We can choose the scale radius a so that the enclosed mass of the NFW and Hernquist profiles is the same for some radius $\tilde{r}$, $M_N(\tilde{r}) = M_H(\tilde{r})$. This implies

$$a/r_s = \left\{[2f(\tilde{x})]^{-1/2} - (1/\tilde{x})\right\}^{-1}, \tag{A11}$$

where $\tilde{x} \equiv \tilde{r}/r_s$. The corresponding total mass of the Hernquist profile satisfies

$$M_H/M_{\rm vir} = (a/r_s)^2/[2f(c_{\rm vir})] \tag{A12}$$

If we choose $\tilde{x} = c_{200}$, then the NFW and Hernquist profiles have the same enclosed mass M_{200} within r_{200}.[11]. We denote by a_{200} the corresponding value of a from equation (A11), and by $M_{H,200}$ the corresponding value of M_H from equation (A12). If instead we choose $\tilde{x} = c_{\rm vir}$, then the NFW and Hernquist profiles have the same enclosed mass $M_{\rm vir}$ within $r_{\rm vir}$. In this case we denote by $a_{\rm vir}$ the corresponding value of a from equation (A11), and by$M_{H,\rm vir}$ the corresponding value of M_H from equation (A12).

As an example, we consider a halo with $c_{\rm vir} = 10$. This yields $c_{200} = 7.4$, $M_{200}/M_{\rm vir} = 0.84$, $a_{200}/r_s = 2.01$, $M_{H,200}/M_{\rm vir} = 1.36$, $a_{\rm vir}/r_s = 2.09$, and $M_{H,\rm vir}/M_{\rm vir} = 1.46$.

REFERENCES

Barnes, J. E., 2011, Astrophysics Source Code Library, record ascl:1102.027

[11]This is what Springel et al. (2005) aimed to achieve. However, their equation (2) is only an approximation to equation (A11), so they do not actually achieve this equality.

Besla, G., Kallivayalil, N., Hernquist, L., Robertson, B., Cox, T. J., van der Marel, R. P., & Alcock, C. 2007, ApJ, 668, 949

Boylan-Kolchin, M., Besla, G., & Hernquist, L. 2011, MNRAS, 414, 1560

Braun, R., & Thilker, D. 2004, A&A, 417, 421

Brown, T. M., Smith, E., Guhathakurta, P., Rich, R. M., Ferguson, H. C., Renzini, A., Sweigart, A. V., & Kimble, R. A. 2006, ApJL, 636, L89

Brunthaler, A., Reid, M. J., Falcke, H., Greenhill, L. J., & Henkel, C. 2005, Science, 307, 1440

Brunthaler, A., Reid, M. J., Falcke, H., Henkel, C., & Menten, K. M. 2007, A&A, 462, 101

Chapman, S. C., Ibata, R., Lewis, G. F., Ferguson, A. M. N., Irwin, M., McConnachie, A., & Tanvir, N. 2006, 653, 255

Chapman, S. C., et al. 2007, ApJ, 662, L79

Collins, M. L. M., et al. 2009, MNRAS, 396, 1619 (C09)

Corbelli, E., & Salucci, P. 2000, MNRAS, 311, 441

Corbelli, E. & Schneider, S. E. 1997, ApJ, 479, 244

Corbelli, E. 2003, MNRAS, 342, 199

Corbelli, E., Lorenzoni, S., Walterbos, R., Braun, R., & Thilker, D. 2010, A&A, 511, 89

Cox, T. J., & Loeb, A. 2008, MNRAS, 386, 461

Dehnen, W., Binney, J. J. 1998, MNRAS, 298, 387

Dorman, C., et al. 2012, ApJ, submitted

Einasto, J., & Lynden-Bell, D. 1982, MNRAS, 199, 67

Evans, N. W., Wilkinson, M. I., Guhathakurta, P., Grebel, E. K., Vogt, S. S. 2000, ApJ, 540, L9

Fardal, M. A., Babul, A., Geehan, J. J., & Guhathakurta, P. 2006, MNRAS, 366, 1012

Fardal, M. A., Guhathakurta, P., Babul, A., & McConnachie, A. W. 2007, MNRAS, 380, 15

Fardal, M. A., Babul, A., Guhathakurta, P., Gilbert, K., & Dodge, C. 2008, ApJ, 682, L33

Ferguson, A. M. N., Gallagher, J. S., & Wyse, Rosemary F. G, 2000, AJ, 120, 821

Galleti, S., Bellazzini, M., Federici, L., & Fusi Pecci, F. 2005, A&A, 436, 535 (G05)

Galleti, S., Bellazzini, M., Federici, L., Buzzoni, A., & Fusi Pecci, F. 2007, A&A, 471, 127 (G07)

Geehan, J. J., Fardal, M. A., Babul, A., & Guhathakurta, P. 2006, MNRAS, 366, 996

Ghez, A. M., et al. 2008, ApJ, 689, 1044

Gilbert, K. M. 2007, ApJ, 668, 245

Gilbert, K. M., Guhathakurta, P., Kollipara, P., Beaton, R. L., Geha, M. C., Kalirai, J. S., Kirby, E. N., Majewski, S. R., Patterson, R. J. 2009, ApJ, 705, 1275

Gillessen, S., Eisenhauer, F., Trippe, S., Alexander, T., Genzel, R., Martins, F., & Ott, T. 2009, ApJ, 692, 1075

Gott, J. R., & Thuan, T. X. 1978, ApJ, 223, 426

Guhathakurta, P., Ostheimer, J. C., Gilbert, K. M., Rich, R. M., Majewski, S. R., Kalirai, J. S., Reitzel, D. B., & Patterson, R. J. 2005, ArXiv e-prints, astro-ph/0502366

Guhathakurta, P., et al. 2006, AJ, 131, 2497

Guo, Qi, White, S. D. M., Li, C., & Boylan-Kolchin, M. 2010, MNRAS, 404, 1111

Ibata, R., Chapman, S., Ferguson, A. M. N., Irwin, M., Lewis, G. F., & McConnachie, A. W. 2004, MNRAS, 351, 117

Ibata, R., Martin, N. F., Irwin, M., Chapman, S., Ferguson, A. M. N., Lewis, G. F., & McConnachie, A. W. 2007, ApJ, 671, 1591

Irwin, M. J., Ferguson, A. M. N., Ibata, R. A., Lewis, G. F., & Tanvir, N. R. 2005, ApJL, 628, L105

Jarosik, N. et al. 2011, ApJS, 192, 14

Kahn, F. D., & Woltjer, L. 1959, ApJ, 130, 705

Kalirai, J. S., Guhathakurta, P., Gilbert, K. M., Reitzel, D. B., Majewski, S. R., Rich, R. M., Cooper, M. C., 2006a, ApJ, 641, 268

Kalirai, J. S., et al. 2006b, ApJ, 648, 389

Kerr, F. J., & Lynden-Bell, D. 1986, MNRAS, 221, 1023

Klypin, A., Zhao., H. S., & Somerville, R. S. 2002, 573, 597

Klypin, A., Trujillo-Gomez, S., Primack, J. 2011, ApJ, in press [arXiv:1002.3660]

Koch, A., & Grebel, E. K. 2006, AJ, 131, 1405

Kochanek, C. S. 1996, ApJ, 457, 228

Kroeker, T. L., & Carlberg, R. G. 1991, ApJ, 376, 1

Lewis, G. F., Ibata, R. A., Chapman, S. C., McConnachie, A., Irwin, M. J., Tolstoy, E., & Tanvir, N. R. 2007, MNRAS, 375, 1364

Li, Y.-S., & White, S. D. M. 2008, MNRAS, 384, 1459

Loeb, A., Reid, M. J., Brunthaler, A., & Falcke, H. 2005, ApJ, 633, 894

Lynden-Bell, D. 1981, The Observatory, 101, 111

Lynden-Bell, D. 1999, in "The stellar content of Local Group galaxies", Proc. IAU Symp. 192, Whitelock, P., & Cannon, R., eds., p. 39 (San Francisco: Astronomical Society of the Pacific)

Majewski, S. R., et al. 2007, ApJL, 670, L9

Martin, N. F., et al. 2009, ApJ, 705, 758

Mateo, M, Olszewski, E. W., & Walker, M. G. 2008, ApJ, 675, 201

McConnachie, A. W., Irwin, M. J., Ibata, R. A., Ferguson, A. M. N., Lewis, G. F., & Tanvir, N. 2003, MNRAS, 343, 1335

McConnachie, A. W., Irwin, M. J., Ferguson, A. M. N., Ibata, R. A., Lewis, G. F., & Tanvir, N. 2004, MNRAS, 350, 243

McConnachie, A. W., Irwin, M. J., Ferguson, A. M. N., Ibata, R. A., Lewis, G. F., & Tanvir, N. 2005, MNRAS, 356, 979

McConnachie, A. W., & Irwin, M. J. 2006, MNRAS, 365, 902

McConnachie, A. W. et al. 2008, ApJ, 688, 1009

McConnachie, A. W. et al. 2009, Nature, 461, 66

McGaugh, S. S. 2005, ApJ, 632, 859

McMillan, P. J., & Binney, J. J. 2010, MNRAS, 402, 934

McMillan, P. J. 2011, MNRAS, 414, 2446

Merrett, H. R., et al. 2006, MNRAS, 369, 120

Navarro, J. F., Frenk, C. S., White, S. D. M. 1997, ApJ, 490, 493

Neto, A. F., et al. 2007, MNRAS, 381, 1450

Peebles, P. J. E., Phelps, S. D., Shaya, E. J., & Tully, R. B. 2001, ApJ, 554, 104

Raychaudhury, S., & Lynden-Bell, D. 1989, MNRAS, 240, 195

Reid, M. J., & Brunthaler, A. 2004, ApJ, 616, 872

Reid, M. J., et al. 2009, ApJ, 700, 137

Sandage, A. 1986, ApJ, 307, 1

Schŕirich, R., Binney, J., & Dehnen, W. 2010, MNRAS, 403, 1829

Shattow, G., & Loeb, A., 2009, MNRAS, 392, L21

Sohn, S. T., Anderson, J., & van der Marel, R. P. 2012, ApJ, submitted (Paper I)

Stadel, J. G. 2001, Ph.D. thesis "Cosmological N-body simulations and their analysis", University of Washington

Tollerud, E., et al. 2012, ApJ, submitted [arXiv:1112.1067v1]

van den Bergh, S. 1998, AJ, 116, 1688

van den Bergh, S. 2000, The Galaxies of the Local Group (Cambridge: Cambridge University Press)

van der Marel, R. P., Alves, D. R., Hardy, E., & Suntzeff, N. B. 2002, AJ, 124, 2639

van der Marel, R. P., & Guhathakurta, P. 2008, ApJ, 678, 187 (vdMG08)

Wang, L., Li, C., Kauffmann, G., & De Lucia, G. 2006, MNRAS, 371, 537

Watkins, L. L., Evans, N. W., & An, J. H. 2010, MNRAS, 406, 264

Zaritsky, D., Olszewski, E., Schommer, R., Peterson, R., Aaronson, M. 1989, ApJ, 345, 759

Zaritsky, D., & White, S. D. M. 1994, ApJ, 435, 599

This preprint was prepared with the AAS LaTeX macros v5.2.

Table 1. M31 Transverse Velocity: Proper Motions and Internal Kinematics

		Spheroid Field	Disk Field	Stream Field
HST PM Measurements				
v_W (HST)	km/s	-167.2 ± 60.2	-194.6 ± 89.8	-65.3 ± 101.5
v_N (HST)	km/s	-137.2 ± 56.2	-38.0 ± 89.1	-130.3 ± 99.3
M31 Internal Kinematics Model				
f (base)		0.738	0.922	0.195
f (GSS)		0.262	0.078	0.805
$v_{\rm LOS}$ (base)	km/s	-1.1	219.8	4.8
$v_{\rm LOS}$ (GSS)	km/s	71.9	-82.3	-185.0
$v_{\rm LOS}$ (all)	km/s	18.0	196.3	-148.0
v_W (base)	km/s	11.0	-25.9	12.0
v_W (GSS)	km/s	22.7	-82.6	73.4
v_W (all)	km/s	14.1	-30.3	61.4
v_N (base)	km/s	-14.3	-49.3	-7.1
v_N (GSS)	km/s	2.5	41.8	157.5
v_N (all)	km/s	-9.9	-42.2	125.4
M31 COM Motion (HST PMs + Internal Kinematics Model + Viewing Perspective)				
v_W (COM)	km/s	-179.1 ± 64.1	-158.0 ± 92.4	-126.3 ± 103.6
v_N (COM)	km/s	-122.6 ± 60.0	-0.5 ± 91.3	-247.5 ± 102.1

Note. — Kinematical quantities for the three HST fields observed in Paper I. The top part of the table lists the HST PM measurements, transformed to km/s using $D = 770 \pm 40$ kpc. The middle part gives the predictions of the M31 internal kinematics model described in Section 2. Predictions are split into two components, the "base" equilibrium galaxy model (disk, bulge, and halo), and the accreted "GSS" tidal stream component. The fraction f gives the amount contributed by each component. Predictions for all model stars (independent of component), are also listed (i.e., averages suitably weighted by the corresponding fractions f). Average velocities are given in the line-of-sight (LOS), West, and North directions. The directions are defined at the center of each field. The internal kinematics velocities are expressed in a frame in which M31 is at rest. The bottom part of the table gives the estimates for the center-of-mass (COM) motion of M31 that result from correcting the HST measurements for both internal kinematics and the viewing perspective. For the COM velocities, the West and North directions are always defined at the COM.

Table 2. Addition to vdMG08 M31 Satellite Galaxy Sample

Name	Type	ρ deg	Φ deg	$v_{\rm los}$ km/s
(1)	(2)	(3)	(4)	(5)
B517	GC	3.29	77.48	-272 ± 54 (G07)
Mac-GC1	GC	3.39	-115.38	-219 ± 15 (G07)
B514	GC	4.04	-145.58	-456 ± 23 (G05)
EC4	GC	4.39	135.88	-288 ± 2 (C09)
B516	GC	4.76	28.44	-181 ± 5 (G07)
B518	GC	5.74	-110.08	-200 ± 48 (G07)
And XV	dSph	6.84	114.86	-323 ± 1 (T12)
B519	GC	7.35	165.67	-268 ± 47 (G07)
And XI	dSph	7.50	174.23	-462 ± 4 (T12)
And XIII	dSph	8.46	166.90	-185 ± 2 (T12)
Mar-GC1	GC	8.50	168.61	-312 ± 17 (G07)
And XXI	dSph	9.00	-78.35	-361 ± 6 (T12)
And XVI	dSph	9.50	158.04	-367 ± 3 (T12)
And XXII	dSph	16.06	141.60	-127 ± 3 (T12)

Note. — The sample of additional M31 satellites, which was combined with the sample from Table 1 of vdMG08 for the modeling of Section 3.1. Column (1) lists the name of the object and column (2) its type. Objects labeled "GC" are distant globular clusters. Columns (3) and (4) define the position on the sky: ρ is the angular distance from M31 and Φ is the position angle with respect to M31 measured from North over East, calculated from the sky positions (RA,DEC) as in van der Marel et al. (2002). The satellites in the table are sorted by their value of ρ. Column (5) lists the heliocentric line-of-sight velocity and its error. The source of the measurement is listed in parentheses — Collins et al. (2009): C09; Tollerud et al. (2012): T12; Galleti et al. (2005): G05; Galleti et al. (2007): G07. Sky positions were obtained from the listed sources or the NASA Extragalactic Database.

Table 3. M31 Center-of-Mass Heliocentric Velocity Estimates

Method	$v_{\rm LOS}$ km/s	v_W km/s	v_N km/s
(1)	(2)	(3)	(4)
HST PMs + Internal Kinematics Model + Viewing Perspective (Section 2)			
Spheroid Field	...	-179.1 ± 64.1	-122.6 ± 60.0
Disk Field	...	-158.0 ± 92.4	-0.5 ± 91.3
Stream Field	...	-126.3 ± 103.6	-247.5 ± 102.1
Weighted Av.	...	-162.8 ± 47.0	-117.2 ± 45.0
Analysis of Satellite LOS Kinematics (Section 3)			
M31 Satellites	-279.3 ± 16.4	-176.1 ± 144.1	8.4 ± 85.4
M33 PM	-183.1 ± 84.9	-47.7 ± 88.2	70.9 ± 91.5
IC 10 PM	-346.1 ± 84.8	-16.2 ± 88.0	-47.3 ± 89.3
Outer LG Galaxies	-361.3 ± 83.6	-140.5 ± 58.0	-102.6 ± 52.5
Weighted Av.	-281.1 ± 15.6	-97.0 ± 40.7	-45.1 ± 36.6
All methods combined			
Weighted Av.	...	-125.2 ± 30.8	-73.8 ± 28.4

Note. — Estimates of the heliocentric velocity of the M31 COM from different methods, as indicated in column (1). The top part of the table gives the results from the HST PM measurements, corrected for internal kinematics as described in Section 2. The weighted average of the results from the three different HST fields is listed as well. The middle part of the table gives the results from the updated vdMG08 analysis, based on the kinematics of M31 and LG satellite galaxies, as described in Section 3. The weighted average of the four independent estimates is listed as well. Column (2) lists the estimated M31 systemic line-of-sight velocities (the actual velocity measured directly from M31 itself is known to be -301 ± 1 km/s; vdMG08). Columns (3) and (4) list the estimated M31 transverse velocities in the West and North directions, respectively. The bottom line of the table lists the weighted average of the two weighted averages from the different methods. This is the final result used in the remainder of our study.

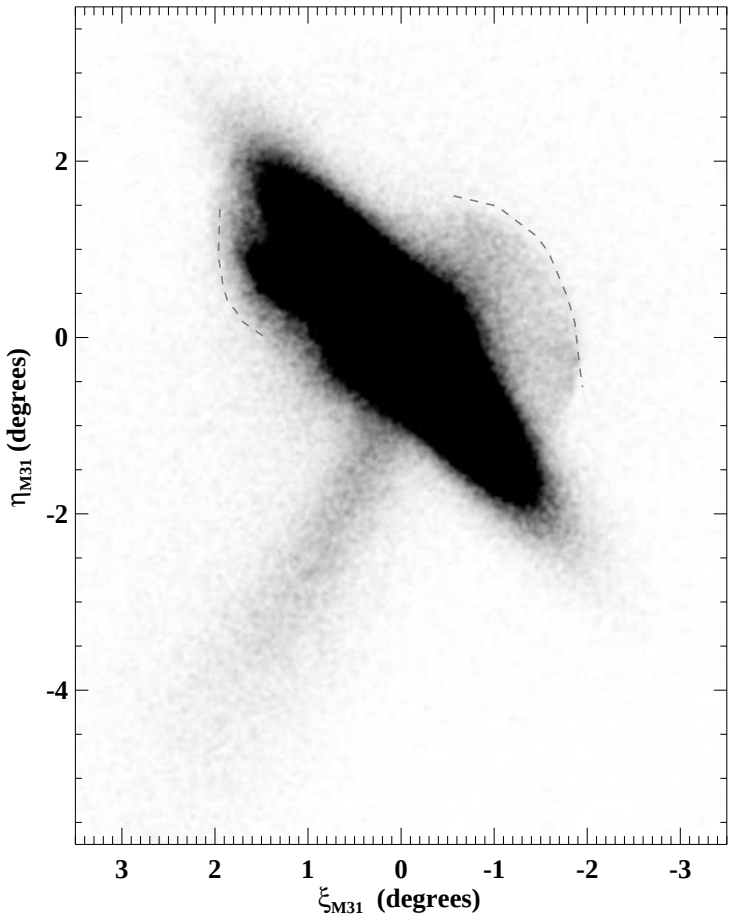

Fig. 1.— Smoothed projected view of the N-body model used to calculate the internal M31 PM kinematics for our HST fields from Paper I. A standard sky projection is used, with North up and East to the left. The GSS is visible South-East of the galaxy center, and the observed positions of the North-East and Western shelf are shown with dashed outlines. This image can be compared to star count maps of giant stars in M31, such as that reproduced in Figure 1 of Paper I, which show very similar features.

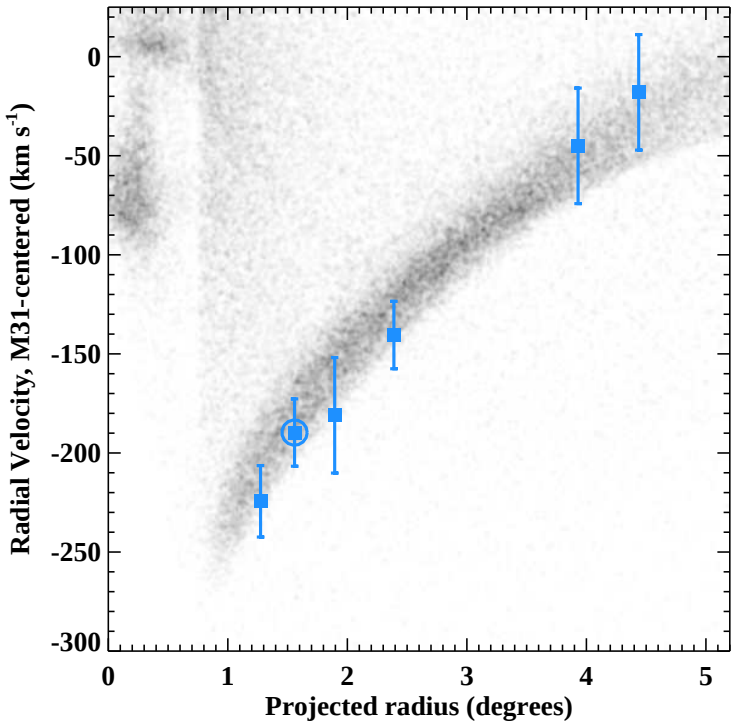

Fig. 2.— Smoothed view in LOS velocity vs. projected distance space of the N-body model used to calculate the internal M31 PM kinematics for our HST fields from Paper I. Only particles with $Y < -0.75°$ are shown (located South-East of the galaxy center), where Y is a cartesian coordinate along the projected galaxy minor axis. The dark band in the figure is due to the GSS, while the base galaxy contributes most of the remaining particles. The GSS location matches the observed peak LOS velocity of the GSS as a function of radius (blue points; Ibata et al. 2004; Guhathakurta et al. 2006; Kalirai et al. 2006a; Gilbert et al. 2009), including that measured in the HST stream PM field of Paper I (circle).

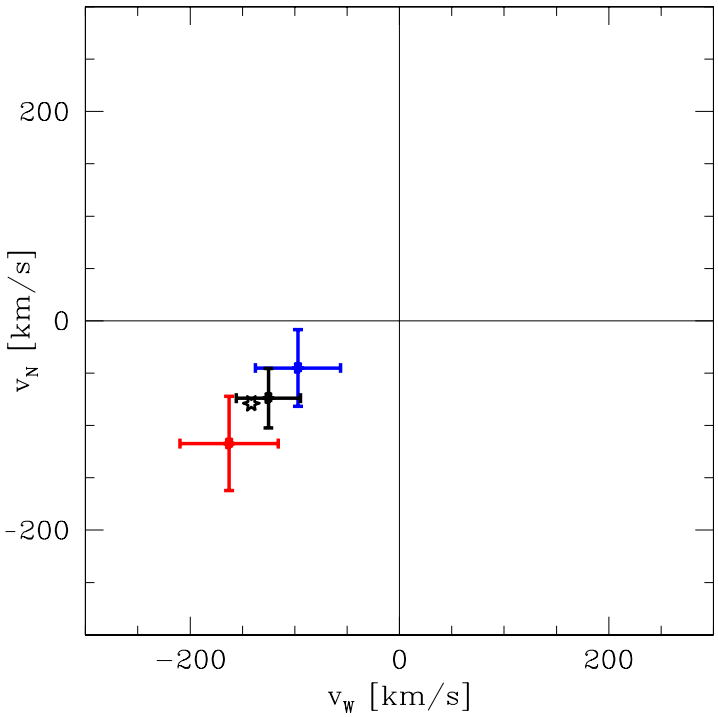

Fig. 3.— Estimates of the M31 heliocentric transverse velocity in the West and North directions. Data points with error bars are from Table 3. Red: Weighted average of HST proper-motion measurements, corrected for internal kinematics (Section 2). Blue: Weighted average of methods based on satellite kinematics (update of vdMG08 result; Section 3). Black: Overall weighted average of all measurements. The starred symbol indicates the transverse velocity that corresponds to a radial orbit for M31 with respect to the Milky Way. The measurements are consistent with a radial orbit.

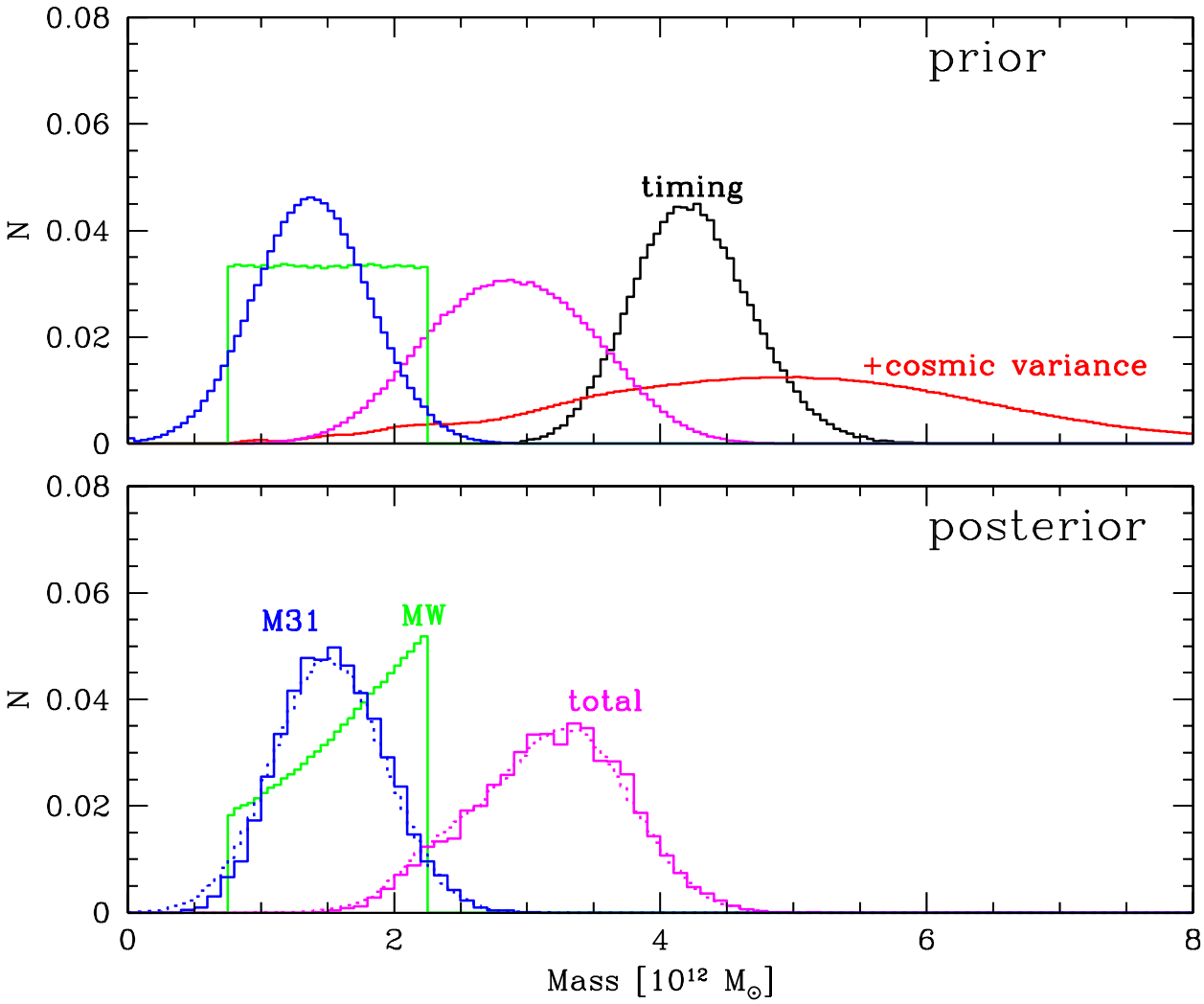

Fig. 4.— Probability distributions for the mass of the Milky Way, M31, and their sum $M_{\rm tot}$. The top panel shows prior probability distributions based on several lines of evidence. M31 (blue) and MW (green): probability distributions based on studies of these galaxies as discussed in the text; Sum of M31 and MW (magenta); Timing argument $M_{\rm tot}$ with inclusion of observational errors (black), and with additional inclusion of cosmic variance from Li & White (2008; red). The bottom panel shows with the same color coding posterior probability distributions, obtained by combining constraints as described in the text. Dotted: knowledge of the individual galaxies combined with the the timing argument; the timing argument does not help much to constrain the masses, due to its large cosmic variance. Solid: Requiring also that M33 and M31 be a bound pair; this reduces the probability of low M31 masses.